

Shape deformations and instabilities of single bubble rising in liquid metals

Original

Shape deformations and instabilities of single bubble rising in liquid metals / Corrado, Marino. - In: PHYSICS OF FLUIDS. - ISSN 1089-7666. - ELETTRONICO. - 34:10(2022), pp. 1-14. [10.1063/5.0102756]

Availability:

This version is available at: 11583/2972348 since: 2022-10-19T08:08:57Z

Publisher:

AIP Publishing

Published

DOI:10.1063/5.0102756

Terms of use:

This article is made available under terms and conditions as specified in the corresponding bibliographic description in the repository

Publisher copyright

AIP postprint/Author's Accepted Manuscript e postprint versione editoriale/Version of Record

This article may be downloaded for personal use only. Any other use requires prior permission of the author and AIP Publishing. This article appeared in PHYSICS OF FLUIDS, 2022, 34, 10, 1-14 and may be found at <http://dx.doi.org/10.1063/5.0102756>.

(Article begins on next page)

Shape deformations and instabilities of single bubble rising in liquid metals

Cite as: Phys. Fluids **34**, 104101 (2022); <https://doi.org/10.1063/5.0102756>

Submitted: 12 June 2022 • Accepted: 30 August 2022 • Accepted Manuscript Online: 01 September 2022
• Published Online: 03 October 2022

 Marino Corrado



View Online



Export Citation



CrossMark

ARTICLES YOU MAY BE INTERESTED IN

[Statistical properties of three-dimensional Hall magnetohydrodynamics turbulence](#)

Physics of Fluids **34**, 095135 (2022); <https://doi.org/10.1063/5.0107434>

[Wake asymmetry weakening in viscoelastic fluids: Numerical discovery and mechanism exploration](#)

Physics of Fluids **34**, 093101 (2022); <https://doi.org/10.1063/5.0100430>

[Breakup of a laminar liquid jet by coaxial non-swirling and swirling air streams](#)

Physics of Fluids **34**, 093606 (2022); <https://doi.org/10.1063/5.0100456>

Physics of Fluids
Special Topic: Cavitation

Submit Today!



Shape deformations and instabilities of single bubble rising in liquid metals

Cite as: Phys. Fluids **34**, 104101 (2022); doi: [10.1063/5.0102756](https://doi.org/10.1063/5.0102756)

Submitted: 12 June 2022 · Accepted: 30 August 2022 ·

Published Online: 3 October 2022



View Online



Export Citation



CrossMark

Marino Corrado^{a)}

AFFILIATIONS

Politecnico di Torino, Department of Energy, Corso Duca degli Abruzzi 24, 10129 Turin, Italy

^{a)} Author to whom correspondence should be addressed: oniram98@gmail.com

ABSTRACT

In this study, a computational fluid dynamics simulation was used to study single bubble flow in liquid metal. Until now, bubble trajectory and shape [Mougin, G. and Magnaudet, J., “Path instability of a rising bubble,” Phys. Rev. Lett. **88**, 014502 (2002)] stability problems in liquid metal have only been insufficiently analyzed in the literature. Because of the difficulty of such an experimental validation, no universal correlations on terminal velocity, shape aspect ratio, and drag force coefficient have been produced to date. The existing bubble shape parameter and terminal velocity correlations with dimensionless numbers are still debatable, mostly because experimental validation is very challenging. The objective of this study was to develop new correlations between bubble stability and bubble deformation in liquid metals. An in-house code, PSI-BOIL, has been used for the simulations. A single bubble rising in a quiescent liquid has been simulated for three different sets of materials (nitrogen+mercury, argon+GaInSn, and argon+steel). The obtained results suggest that shape instability phenomena take place in the bubble dynamics in liquid metals for Eötvös numbers >1.7 . Small bubbles ($Eo < 1.7$) maintain a stable ellipsoidal shape, while the shape and velocity of larger bubbles ($Eo > 1.7$) tend to oscillate with bubbles rising via non-rectilinear trajectories. The inviscid approximation works well for bubbles in liquid metals. It has been confirmed that the dynamics and the shape of small bubbles ($Eo < 1.7$) in liquid metals are only controlled by the Weber number.

Published under an exclusive license by AIP Publishing. <https://doi.org/10.1063/5.0102756>

NOMENCLATURE

D	Bubble diameter (m)
F	Force (N)
g	Gravitational acceleration (m/s^2)
p	Pressure (Pa)
t	Time (s)
u	Velocity (m/s)
u_T	Terminal rising velocity (m/s)
X	Bubble aspect ratio: bubble height divided by bubble width (-)
γ	Surface tension coefficient (N/m)
μ	Dynamic viscosity (Pa s)
ρ	Density (kg/m^3)
χ	Curvature (m^{-1})

Dimensionless numbers

Eo	Eötvös number, $Eo = \frac{(\rho_l - \rho_g)gd^2}{\gamma}$
Mo	Morton number, $Mo = \frac{g\mu_l^4(\rho_l - \rho_g)}{\rho_l\gamma^3}$

Re Reynolds number, $Re = \frac{\rho_l u_T D}{\mu_l}$

We Weber number, $We = \frac{\rho_l u_T D}{\gamma}$

Subscript

a	Archimede
g	Gas
i	Inertia
l	Liquid
st	Surface tension
v	Viscous

INTRODUCTION

Bubble motion in liquid metals plays a determining role in many engineering processes. Gas bubbles are commonly inserted into a liquid metal to enhance the mixing process that takes place in the liquid phase (Liu and Li, 2017) and to improve the heat transfer of the liquid (Lorenzin and Abánades, 2016). In fact, liquid metal is an excellent type of energy carrier, and it is largely used in many types of nuclear

reactors, such as fast reactors, spallation source devices, and fusion reactors.

Moreover, a bubbly flow in liquid metal is also used in industrial processes, such as in metal stirring and purification, continuous casting, and liquid metal chemical reactions, with the purpose of increasing efficiency. A great deal of scientific research has been carried out in this field. In continuum casting (Liu and Li, 2017), for example, bubbles are injected into a liquid metal to avoid clogging of the flow and to make the process as continuous as possible. Timmel *et al.* (2010) presented a new experimental facility (LIMMCAST) focused on the study of gas bubble rising in metals. Yang *et al.* (2020) produced an advanced breakup/coalescence model to precisely predict bubbles flow in liquid metals. Baake *et al.* (2017) demonstrates the effectiveness of neutron radiography for the experimental investigation of these phenomena.

Because of its innumerable industrial applications, bubble motion in liquid metal has been a central topic for the scientific community over the past 70 years (Haas *et al.* 2021). Nevertheless, important questions, concerning the stability and velocity of bubbles in this range, still remain unclear and the bubble rising problem remains an open issue in multi-phase fluid mechanics. In particular, no correlations between bubble shape and velocity have been revealed to be accurate in a liquid metal.

Bubble rising in a quiescent liquid is a well-known problem in multiphase-fluid mechanics.

Moreover, correlations between fluid-dynamics dimensionless numbers have been produced in the literature for a wide range of Eötvös and Reynolds numbers, but a universal correlation has not yet been found. Nevertheless, many correlations, which are valid over their own ranges, were derived or produced in the past.

Levich (Kang and Leal, 1988) analytically derived a drag coefficient that is valid for a inviscid flow [viscosity tends to zero ($\mu \rightarrow 0$)] for spherical bubbles [aspect ratio tends to unity ($X \rightarrow 1$)] in which the viscous component of the drag force is negligible (high Re).

Hadamard (1911) derived a drag coefficient for a creeping flow ($Re < 1, X \rightarrow 1$), assuming that the pressure component by the wake is negligible. Mei and Klausner (Tomiyama *et al.*, 1998) extended Hadamard's correlation for spherical bubbles to an arbitrary Reynolds number.

Mendelson (1967) studied the bubble rising problem in inviscid liquid and approximated the bubble velocity to that of the propagation wave velocity of the gas-liquid interface. The phase velocity, u_{phase} , is assumed to be the sum of the velocity resulting from the surface tension and the gravitational term.

The aforementioned author computed the bubble rising velocity by determining the principal wavelength, $\lambda = \pi d$.

Tomiyama *et al.* (1998) generalized the drag correlation for a wider range ($10^{-2} < Eo < 10^3, 10^{-14} < Mo < 10^7, 10^{-3} < Re < 10^5$) and provided the most general correlation possible. First, he unified Levich and Hadamard's correlation for a wide range of Reynolds numbers. He then calculated the drag coefficient, using Mendelson's theory, to provide a drag coefficient that is only dependent on the initial conditions. Since a bubble no longer tends to be spherical for higher Eo , but is instead ellipsoidal, the terminal velocity is lower than in a spherical case. The maximum of the two drag coefficients is chosen by considering this effect. Yan *et al.* (2018) produced a more precise empirical solution for the bubble drag coefficient for the

same range of correlations as Tomiyama. Zhou *et al.* (2020) produced a novel correlation for the drag coefficient of a bubble rising in liquid, which predicts 93.5% of the available existing data.

The main issue in finding a universal correlation is the large scale of change of the dimensionless numbers (Re, Eo, Mo), that is, of several orders of magnitude. Viscous, inertia, and tension forces have different degrees of importance in each region in the Grace diagram (Acrivos, 1979), and the bubble behavior changes to a great extent. Thanks to experiments and computational fluid dynamics (CFD) simulations, a map has been created, which predicts the terminal Reynolds number, once the initial conditions are known. Generally, the bubble terminal Reynolds number increases as the Eötvös number increases and decreases as the Morton number decreases.

The deformation of the bubble shape has also been a widely studied topic over the last few decades because of its numerous industrial (Liu and Li, 2017) and research applications. Experiments and CFD simulations have led to the formation of maps that describe different types of bubble shape in different dimensionless number regimes (Krull *et al.*, 2016). The shape of a bubble is controlled by two dimensionless numbers, as is its velocity. The most common numbers used in the literature are the Reynolds number and the Eötvös number. A bubble with $Re < 1$ tends to keep a spherical shape for all Eo . Such a bubble gradually changes from spherical to ellipsoidal and finally to a spherical cap shape for higher Reynolds numbers ($Re > 1$), thereby increasing the Eötvös number. Furthermore, the bubble shape is highly sensitive to the initial flow condition (Tomiyama *et al.*, 2002). A non-zero velocity field or a residual initial compression of a bubble can easily lead to a different kind of bubble rising behavior (different trajectory and different shape). Many correlations, based on experimental and CFD data, are present in the literature, each with its own range of validity.

Besagni and Deen (2020) compared the most famous shape correlations present in the literature and provided his own new correlation, which is the most accurate generalization to date, based on the many experimental data he had available.

Moore (1959) analytically predicted the bubble shape in liquid metal through a linear theory, which, however, loses precision for large bubbles. Sugihara (Besagni and Deen, 2020) extended Moore's correlation to a wider range of Weber numbers. The effectiveness of the latter two correlations is based on assuming that the flow in liquid metals behaves like an inviscid flow. Therefore, the dynamics is controlled entirely by the Weber number. Legendre *et al.* (2012) extended Moore's correlation to more viscous fluids ($1 < \log Mo < 11$), focusing the study on the bubble-liquid interfacial area.

Aoyama *et al.* (2016) experimentally studied bubble deformation for specific Morton numbers ($\log Mo = -6.6, -5.5, -4.9, -3.9$) and produced a correlation for shape deformation for a wide range of Morton numbers. Zhou *et al.* (2020) also studied the bubble deformation problem and produced the most general correlation for the bubble aspect ratio, which agrees with 90% of the existing experimental and numerical data.

Gaudlitz and Adams (2009) investigated bubble path and find a connection between the trajectory and wake structure.

Zhang and Ni (2014) discovered vertical uniform magnetic field can straighten the bubble trajectory and found a close relationship between fluctuations in rising velocity and shape variations. He (Zhang *et al.*, 2016) also investigated bubble velocity and shape under

the horizontal magnetic field. In this case, the magnetic field tends to decompress bubble shape, straighten the trajectory, and exponentially reduce the terminal velocity.

Both Zhou and Dušek (2017) and Cano-Lozano et al. (2013) proposed a marginal stability curve of a deformable bubble ascending freely in a viscous Newtonian liquid.

Schwarz and Fröhlich (2014) investigated bubble rising under the magnetic field and, in accordance with Zhang studies, produced a correlation between the horizontal magnetic field and terminal velocity for a wide bubble range.

Zhang et al. (2021) recently demonstrated the mechanism to control the trajectory of an air bubble under the application of a magnetic field

Will et al. (2021) experimentally investigated the effect of geometrical anisotropy for buoyant spheroidal particles rising in a still fluid and discovered bubble shape and trajectory are highly dependent on initial bubble compression.

As the Eötvös number increases, a bubble starts to experience instability phenomena that influence the trajectory, the velocity, and the shape of the bubble itself. The stability of a bubble is influenced by the ratio of the surface tension forces ($\sim D^2$) to the inertia forces ($\sim D^3$). The bubble starts to experience 3D dependent forces, and it loses its axial symmetry, and this renders the bubble rise a more complex phenomenon. Certain large bubbles in low Morton number regions ($Mo < 10^{-4}$) experience instabilities and the bubble changes shape from ellipsoidal to a wobbling disk. The reason why these instabilities occur has not yet been ascertained completely. Many authors, such as Mougin and Magnaudet (2002), asserted that the main cause of the onset of these instability phenomena are wake vortices that appear under the bubble. Those vortices increase the energy dissipation and the flow field on the bottom of the bubble, which loses its axisymmetry, and this, in turn, leads to the onset of instabilities.

As can be seen in Fig. 1, a liquid metal is a region for which no universal correlation has yet been found. The main obstacle is the opacity of the metal that makes an optical inspection of the bubble almost impossible. In the past, such techniques as the electrical triple probe (Mori et al., 1977) were adopted to determine the bubble rising velocity. Nevertheless, due to inaccuracies of the instrumentation, it was not possible to precisely predict the bubble velocity, and only overall estimates could be obtained. Modern techniques, such as UDV (Ultrasound Doppler Velocimetry), Neutron radiography (Wang et al., 2017), and x-ray radiography, seem to be the best tools to experimentally investigate this environment.

Keplinger et al. (2017) validated x-ray radiography as an inspection technique for comparing his data with results in water and used it to experimentally study bubble breakup (Keplinger et al., 2019) and coalescence (Keplinger et al., 2018) in liquid metals.

Strumpf (2017) and Zhang et al. (2005) adopted UDV to investigate bubble velocity and trajectory under the magnetic field, while Richter et al. (2018) experimentally studied path and shape instabilities by mean of x-ray radiography.

Birjukovs et al. (2020; 2021) demonstrated a new image processing methodology for resolving gas bubbles traveling through liquid metal from dynamic neutron radiography and adopted it for studying high Reynold bubble rising. Until now, all the conducted experiments have been insufficient to produce a robust correlation for the bubble rising velocity, u_∞ , and aspect ratio, X , in liquid metals. These modern

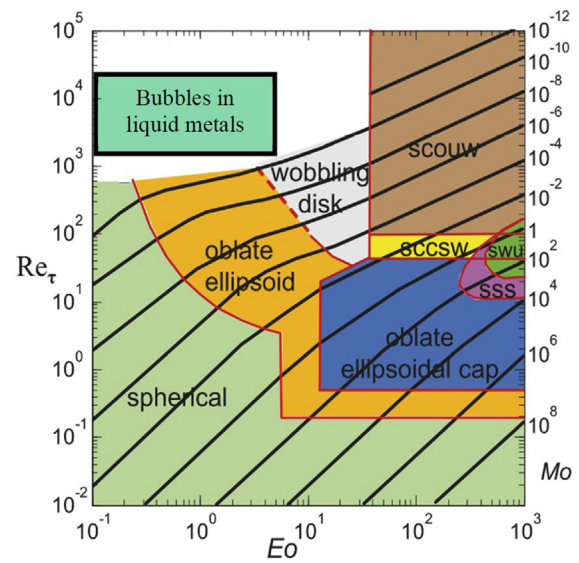


FIG. 1. Region of bubbles in typical liquid metals in the Grace diagram (Jin et al., 2016). Bubble shape: scouw—spherical cap with open unsteady wake; sccsw—spherical cap with closed steady wake; swu—skirt with wavy unsteady skirt; sss—skirt with smooth steady skirt.

techniques show a much higher accuracy in detecting the bubble velocity and shape than the older ones, but they result to be expensive, and their use is somewhat limited.

Objectives of the present study

Bubble stability problems in liquid metal have been insufficiently analyzed in the literature. Because of the difficulty involved in conducting experimental validations, no universal correlations have been produced as yet.

Similarly, deformations of the bubble shape and their terminal velocities in liquid metal are not fully developed topics in fluid dynamics, mostly because of the difficulty in their validation.

As far as the bubble shape in liquid metals is concerned, Moore (1959) proposed the most famous correlation but, because of the important assumptions in this correlation, it loses the applicability for large bubbles and a more general theory is, therefore, required.

In this study, a computational fluid dynamics (CFD) simulation was used to study single bubble flow in liquid metal. More precisely, a new analytic theory on the velocity and deformation of bubble rising has been produced and compared with the CFD results of the PSI-BOIL code. PSI-BOIL is an in-house code developed by the Paul Scherrer Institute (PSI). It is a CFD code specialized in high precision simulation of biphasic heat transfer problems based on the finite discretization technique.

The CFD velocities of bubbles in liquid metals are compared with those obtained by means of the existing correlations in the literature studies. A semi-analytical model for bubble shape deformation is also derived for liquid metal and is compared with the CFD results. Finally, a new stability criterion is proposed for bubbles in liquid metal.

GOVERNING EQUATIONS

The studied problem refers to a single bubble rising in a quiescent liquid metal. The governing equations for the incompressible flow are defined as

$$\nabla \cdot u = 0, \tag{1}$$

$$\frac{\partial(\rho u)}{\partial t} + \nabla \cdot (\rho u \otimes u) = -\nabla p + \nabla \cdot \left(\mu \left(\nabla u + (\nabla u)^T \right) \right) + \rho g + \gamma \chi n, \tag{2}$$

where u (m/s) is the fluid velocity vector, p (Pa) is the pressure, t (s) is the time, ρ (kg/m³) is the density, μ (Pa s) is the dynamics viscosity, g (m/s²) is the gravitational acceleration, γ (N/m) is the surface tension coefficient between the gas and the liquid, χ (N/m) is the local curvature of the interface, and n is the normal vector of the interface.

The energy conservation equation was not solved since the thermal energy exchange was considered negligible. Thus, the temperature field was assumed to be constant, and the material properties of the gas and the liquid were kept constant.

A linear interpolation between liquid and gas was considered, using the volume fraction H , to compute the material properties,

$$\mu = H\mu_1 + (1 - H)\mu_2, \tag{3}$$

$$\rho = H\rho_1 + (1 - H)\rho_2, \tag{4}$$

$$\sigma = H\sigma_1 + (1 - H)\sigma_2. \tag{5}$$

The governing equation for the transport of the volume fraction was written as in Eq. (6), and it was solved with the volume of fluid (VOF) method,

$$\frac{\partial H}{\partial t} + \nabla \cdot (uH) = 0. \tag{6}$$

The continuity and momentum conservation equations were solved using the fractional step method. An adaptive time step was used, where the time step was defined as $\Delta t = \min\{\Delta t_{CFL}, \Delta t_\gamma\}$, where

$$\Delta t_{CFL} = C_{CFL} \frac{\Delta}{|u_{max}|}, \tag{7}$$

$$\Delta t_\gamma = 5 \cdot \sqrt{\frac{0.5 \cdot \rho_{GAS} \cdot \Delta^3}{2\pi\gamma}}, \tag{8}$$

where C_{CFL} is the Courant–Friedrichs–Lewy (CFL) number, and it was set to 0.25 in this study. u , v , and w are the velocity components in the x -, y -, and z -directions, respectively, and Δ is the grid spacing.

Conditions of simulations

A 3D rectangular computational domain, with $6D \times 6D \times 24D$ dimensions (both the lateral directions and the height), was used and was discretized with a uniform cube mesh ($dx = D/16$). The liquid was quiescent at the beginning. The height of $24D$ was sufficient for all the bubbles to reach terminal velocity. The width of $6D$ made the flow independent of the influence of the surrounding walls.

Simulations were conducted with different bubble sizes ($0.1 < Eo < 2$). Three cases of systems with different material combinations were considered: argon–GaInSn, nitrogen–mercury, and argon–iron. These three sets of materials have been used because they are

TABLE I. Material properties for three systems with different combinations of gas and liquid phases.

	μ (Pa s)	ρ (kg/m ³)	γ (N/m)
Argon	1.176×10^{-5}	1.654	0.5330
GaInSn	2.20×10^{-3}	6.36×10^3	
Nitrogen	1.77×10^{-5}	1.17	0.4535
Mercury	1.50×10^{-3}	1.35×10^4	
Argon	1.176×10^{-5}	1.654	1.200
Iron	6.30×10^{-3}	7.00×10^3	

common in metallurgical processes and above all because they have been used in previous experiments and simulations (Moore, 1959), so that the results of PSI-Boil can be compared and validated. The material properties are listed in Table I.

In the beginning of the simulation, the velocity field was zero. The pressure field followed Stevino’s law and increased linearly with the depth. A spherical bubble was placed in the center in the x - and y -directions and at a $2D$ distance from the bottom, as shown in Fig. 2.

ANALYSIS OF BUBBLE DYNAMICS IN LIQUID METAL

Analytical description

Governing parameters

A single bubble rising in liquid metal is characterized by a high Reynolds number, that is, Eq. (9) and considerably low Morton numbers, Eq. (10). The Reynolds number, which was of the order of one thousand, due to the high liquid metal density compared to water, suggests that inertia forces (F_i) were predominant over the viscous forces (F_v) ($Re \gg 1$). The Morton number was particularly low ($\approx 10^{-13}$), which means that the Archimedes (F_a), Eq. (12), and surface tension (F_{st}) forces were dominant over the viscous forces. The two driving factors that characterize bubble rising in liquid metal are the inertia and surface tension forces, while the viscous term, although present, does not play any substantial role,

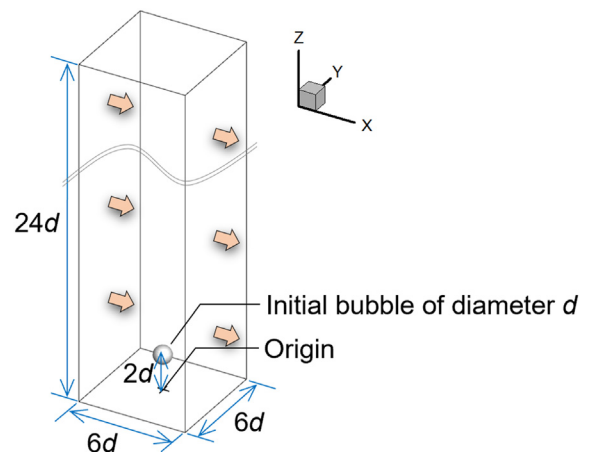


FIG. 2. Computational domain and the initial bubble.

$$Re = \frac{F_i}{F_v} = 10^4, \tag{9}$$

$$Mo = \frac{F_v}{F_{st} * F_a} = 10^{-13}. \tag{10}$$

The system was characterized by only two dimensionless parameters, Eq. (11), in which viscosity was absent, since it no longer had any driving power. The Eötvös number and the Weber number ($We = \frac{\rho v^2 D}{\gamma}$) were used in this analysis,

$$F(\Pi_1, \Pi_2, \Pi_3) = 0 \rightarrow F(We, Eo) = 0 \rightarrow We = F(Eo). \tag{11}$$

Under this approximation, a two-variable function fully characterized the problem. Furthermore, since Eo was not velocity dependent, the bubble rising velocity could be explicitly expressed as a function of the material and geometry properties.

Negligible shear stress field

In a Newtonian fluid, the stress tension is proportional to the velocity gradient $\tau = \mu \cdot \nabla u$. In a solid sphere, since internal flow does not occur, the liquid velocity on the sphere surface is zero and $\tau \cong \mu \cdot \frac{u_{\infty}}{L}$, with L equal to the characteristic decreasing length.

The viscous effect becomes less dominant in bubbles rising in liquid metal. The surface shear stress field on the bubble surface is significantly reduced by two phenomena:

- First, inner gas recirculation takes place, and the bubble surface velocity is no longer zero. Since there is a huge difference in the gas–liquid density, the outermost layer of the gas is carried by the external liquid, which has higher inertia. Therefore, the velocity gradient and the shear stress are significantly reduced to $\tau \cong \mu \cdot \frac{u_{\infty} - u_{surf}}{L}$. This effect is relevant for large bubbles for which there is enough space inside to create convective gas movement.
- Second, the purity of the surrounding liquid increases the slipping effect along the surface of the bubble, thereby further decreasing the local velocity gradient. Both contributions significantly reduce the tension stress field across the bubble interface.

Bubble force balance

Under equilibrium, the buoyancy force, which is velocity independent, Eq. (12), is balanced by the drag force, Eq. (13), which generally increases as the velocity increases. The buoyancy force is the sum of the gravitational force and the surface integral of the static pressure, h , acting on the bubble. The drag force is computed by integrating the pressure ($p_{tot} - p_{static}$) with the shear stress field.

In this analysis, the considered system was the whole bubble, which is the sum of the interface and the inner gas. Since the surface tension is a mutual force that acts between the surface and the inner gas, it was not necessary to consider it since it is an internal force of the system

$$\begin{aligned} F_{buoyancy} &= -mg + \oint p_{static} \cdot d\vec{A} = -\rho_g Vg + \rho_l Vg \\ &= \Delta\rho \cdot V \cdot g = \Delta\rho \cdot \frac{\pi D^3}{6} \cdot g, \end{aligned} \tag{12}$$

$$F_{drag} = \oint (p_{tot} - p_{static}) \cdot d\vec{A} + \oint \tau_{//} \cdot d\vec{A}. \tag{13}$$

The velocity and pressure distribution over the entire bubble surface needs to be known to compute the drag. The pressure and the tension terms are generally equally important, and both need to be computed. The pressure field across the bubble is computed by resolving the Navier–Stokes equations Eq. (14) along a streamline from a distant point to the surface, Eq. (15). The pressure on the bubble surface is the sum of a gravitational, a kinetic, and a viscous term. The gravitation term is not treated since it is already considered in the buoyancy force. The $p_{tot} - p_{static}$ field at the bubble interface is the sum of a kinetic and a viscous pressure, Eq. (15),

$$\rho \left[\frac{\partial u}{\partial t} + u \cdot \nabla u \right] = -\nabla p + \mu \nabla^2 u + \rho g \cdot dz, \tag{14}$$

$$p_{tot} - p_{static} = \frac{\rho}{2} \cdot (u^2(s) - u_{\infty}^2) + \mu \int_{\infty}^s \nabla^2 u \cdot dr. \tag{15}$$

The kinetic pressure in the upper part of the bubble is much larger than the viscous pressure, ($\frac{1}{2} \rho u_{\infty}^2 \gg \mu \int_{\infty}^s \nabla^2 u \cdot dr$), because of the high density of liquid metals and because of the small stress tensor field, $\tau = \nabla u$.

In Fig. 3, \vec{r} represents the streamline of the flow and \vec{s} the position on the bubble surface,

$$\Delta p_v = \mu \int_{\infty}^s \nabla \cdot \vec{\tau} \cdot dr = \mu \int_{\infty}^s \frac{\partial}{\partial s} \tau_s \cdot dr = \mu \int_{\infty}^s \tau_s(r) \cdot dr. \tag{16}$$

- $\tau(\infty)$ is zero and increases as it approaches point A, in which τ reaches its maximum value.
- The tension stress field $\tau(A)$ is negligible, since the velocity changes almost linearly on the side of the bubble due to an efficient internal flow (Analysis of bubble dynamics in liquid metal)
- Therefore, $\int_{\infty}^s \tau_s(r) \cdot dr$ is also negligible and the viscous overpressure is zero.
- Viscous pressure Eq. (16) is negligible for each point in the upper part of the bubble.

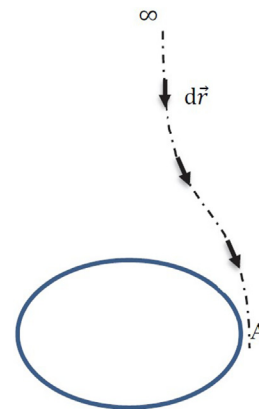


FIG. 3. Flow streamline.

The fluid before the bubble detachment point can be considered inviscid, as there are no energy dissipations, and all the liquid momentum is transferred into pressure, Eq. (17). When the liquid is approaching the bubble surface, the velocity is decreased, and the kinetic energy is changed into pressure energy. The stagnation point of the bubble (top point) has the highest pressure, and when approaching the sides of the bubble, the pressure decreases monotonously. Therefore, the inviscid model was used to model the pressure on the bubble surface. No boundary layer exist, and only the tangential component of velocity $u_{//}$ was present on the bubble surface,

$$\Delta(p_{\text{tot}} - p_{\text{static}}) + \frac{1}{2}\rho\Delta u^2 = 0. \tag{17}$$

How the pressure changes from the stagnation point to the bubble sides depends on the bubble aspect ratio (X), which, in turn, depends on the pressure acting on the surface. Nevertheless, it can be established that the surface pressure field is proportional to the pressure of the stagnation point, which is, according to Bernoulli, equal to $\frac{1}{2}\rho_1 u_\infty^2$. Therefore, kinetic overpressure Eq. (18) depends on bubble velocity u_∞ and on the local velocity tangential to the surface $u(s)$,

$$p_{\text{kinetic}}(s) = \frac{1}{2}\rho(u_\infty^2 - u^2(s)). \tag{18}$$

The inviscid approximation is no longer feasible after the detachment point (Fig. 4). The fluid on the bottom of the bubble is no longer irrotational, and dissipation phenomena take place. The pressure on the bottom of the bubble is significantly reduced, because all the liquid momentum is dissipated by the viscosity friction and does not contribute to hydrodynamic pressure. From the Lagrangian point of view, the fluid particles that are approaching the bubble surface decelerate and their kinetic energy decreases. In an ideal case, the pressure increases to conserve kinetic energy but, due to viscous forces, most of the energy is dissipated and the liquid pressure is drastically reduced, compared the non-viscous case. How much energy is transferred into pressure and how much is lost depends on the velocity field. In this analysis, a total dissipation model is used for simplicity. Therefore, all the kinetic energy of the liquid is dissipated, while the pressure field after the detachment point can be approximated to zero Eq. (19) and has no impact on the drag force (Fig. 5),

$$p_{\text{tot}}(s) - p_{\text{static}}(s) = \frac{1}{2}\rho(u_\infty^2 - u^2(s)) + \mu \int_\infty^s \nabla^2 u \cdot ds \simeq 0. \tag{19}$$

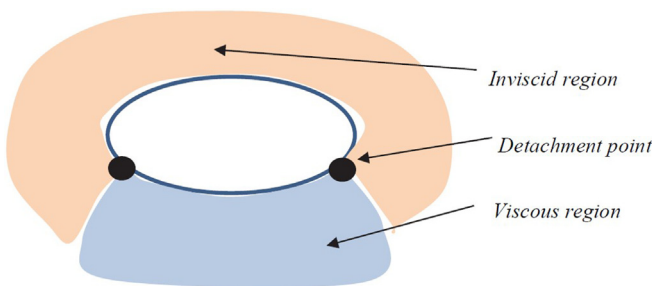


FIG. 4. Top and bottom of the bubble modeled, respectively, with inviscid and viscous model.

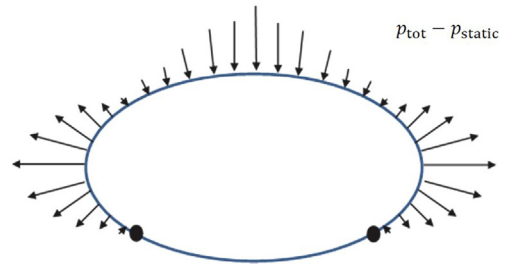


FIG. 5. Pressure field ($p_{\text{tot}} - p_{\text{static}}$) on the bubble surface.

The shear stress component was neglected to compute the drag force, since it was much lower than the pressure component. Moreover, the pressure field was only integrated in the “inviscid region,” since any pressure on the bottom was assumed to be zero due to dissipation, Eq. (20). Moreover, $p_{\text{tot}} - p_{\text{static}}$ in the inviscid region is the kinetic pressure.

Clearly, the viscous pressure was physically the main cause of the drag force but, due to the full dissipation model used at the bottom of the bubble, the liquid viscosity coefficient did not influence the bubble dynamics and the drag force only depended on the kinetic pressure upstream of the detachment point.

The point of detachment of the liquid from the liquid surface depends on the bubble shape and on the kinetic energy density of the liquid (ρu^2). Since the bubble was assumed to be ellipsoidal, it can be assumed, without any loss of generality, that the detachment point depended only on the bubble aspect ratio and on the Weber number of the bubble,

$$\begin{aligned} F_{\text{DRAG}} &= \oint (p_{\text{tot}} - p_{\text{static}}) \cdot d\vec{A} + \oint \tau_{//} \cdot d\vec{A} \simeq \oint p_{\text{kinetic}} \cdot d\vec{A} \\ &= \oint \frac{1}{2}\rho(u_\infty^2 - u^2(s)) \cdot d\vec{A}. \end{aligned} \tag{20}$$

The final balance equation is

$$\Delta\rho \cdot \frac{\pi D^3}{6} \cdot g = \oint \frac{\rho}{2} \cdot (u_\infty^2 - u^2(s)) \cdot d\vec{A}. \tag{21}$$

The liquid velocity on the bubble surface only has the $u_{//}$ component tangential to the surface, while the normal component, u_n , is zero to conserve the flow rate ($\nabla \cdot u = 0$). We assume the local velocity on the surface of the bubble is proportional to the rising bubble velocity. $u^*(s)$ is a unknown function that represents the dependency of the velocity on the local position,

$$u(s) = u^*(s) \cdot u_\infty, \tag{22}$$

$$\Delta\rho \cdot \frac{\pi D^3}{6} \cdot g = \oint \frac{\rho \cdot u_\infty^2}{2} \cdot (1 - u^{*2}(s)) \cdot d\vec{A}, \tag{23}$$

$$\Delta\rho \cdot \frac{\pi D^3}{6} \cdot g = \frac{\rho \cdot u_\infty^2}{2} \cdot \overline{1 - u^{*2}(s)} \cdot \pi D^2, \tag{24}$$

$$Eo = 3 \cdot We \cdot \overline{1 - u^{*2}(s)}, \tag{25}$$

$$\overline{1 - u^{*2}(s)} = g(X(We)) = g(We), \tag{26}$$

$$Eo = 3 \cdot We \cdot g(We), \tag{27}$$

$$F(We, Eo) = 0. \tag{28}$$

As can be seen in Eq. (27), the whole system is characterized by only two dimensionless numbers, which are connected.

Moreover, $1 - u^{*2}(s)$ is the surface average of the $1 - u^{*2}(s)$ function in the inviscid region before the detachment point. Such a function can only be known exactly by resolving the flow and the pressure field around the bubble. Nevertheless, by assuming the bubble is axi-symmetric ellipsoidal shaped, $1 - u^{*2}(s)$ is a function of only the aspect ratio of the ellipsoid ($X = \frac{d}{c}$). In the next section, it is demonstrated that the aspect ratio is only a function of the Weber parameter. This means that the bubble rising problem can be expressed with a single equation that contains only two dimensionless numbers $F(We, Eo)$. Therefore, the whole problem is influenced by only one dimensionless number.

Terminal rising velocity

Comparison against Tomiyama's correlation

The computed Reynolds number, based on the terminal rising velocity, is compared with Tomiyama's correlation Eq. (29) in Fig. 6 as a function of the Eötvös number. The range simulated here corresponds to Mendelson's formula in Tomiyama's correlation, in which the velocity is only controlled by the Eötvös number. It can be observed that, on first approximation, Tomiyama's correlation and, therefore, Mendelson's equation, are able to clearly predict the bubble behavior and give the right order of magnitude of the terminal Reynolds number,

$$C_D = \max \left\{ \min \left[\frac{16}{Re} (1 + 0.15Re^{0.687}), \frac{48}{Re} \right], \frac{8}{3} \cdot \frac{Eo}{Eo + 4} \right\}. \quad (29)$$

There is a rapid change in the velocity profile in Tomiyama's correlation (Fig. 7) when passing from the Eötvös dependent region ($C_D = \frac{8}{3} \cdot \frac{Eo}{Eo+4}$) to the Reynolds dependent region ($C_D = \frac{48}{Re}$). As we consider smaller bubbles, the Reynolds number acquires more importance, while Eo loses importance in determining the drag coefficient. The change from the Eo to Re region is gradual in the simulations, and the velocity slope changes smoothly from negative to positive. The Tomiyama curve has been validated in low-intermediate Reynolds regimes and never in the liquid metal. This could be the reason for significant deviations of CFD results from the Tomiyama correlation.

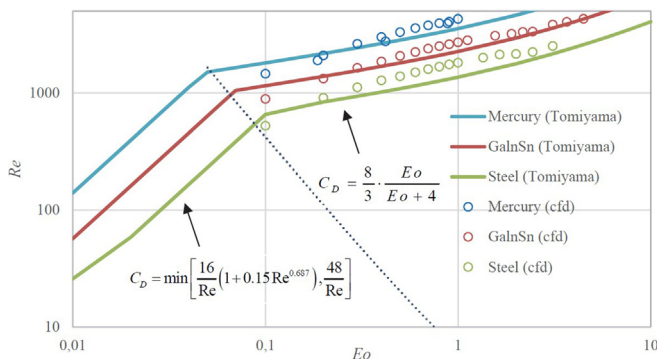


FIG. 6. Comparison between Tomiyama's correlation and PSI-BOIL simulation results.

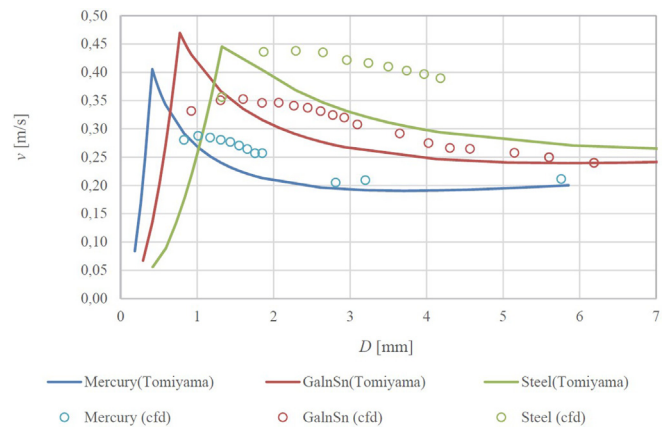


FIG. 7. Comparison of terminal velocity as the function of bubble diameter between Tomiyama's correlation and PSI-BOIL.

Unfortunately, due to a CFD parasitic current issue, it was impossible to simulate bubbles with $Eo < 0.05$. The parasitic current is a computational phenomenon that occurs when there is a low resolution of the surface of the bubble which compromises the accuracy of the shape of the bubble and the resolution of the surface tension force. Once a grid size is set, the simulations are no longer reliable under a certain bubble size.

Therefore, the $C_D = 48/Re$ dependency region cannot be demonstrated by means of simulations.

Instabilities of bubble

A certain number of large bubbles tend to show instable behavior at some points during their rising (Fig. 8). The trajectory is no longer rectilinear, and the instant velocity is kept the same; therefore, the average rising vertical velocity decreases.

Wake flow no longer tends to be axisymmetric and non-uniform velocity oscillations are a direct consequence of bubble shape oscillations initiated by wake flow asymmetrization.

The line in the Grace diagram that separates the stable and unstable bubble regions has a negative slope. This means that, for high Morton numbers, instabilities will occur for larger Eötvös number, while instabilities occur earlier for low Morton material instabilities. The Morton number can be considered a good parameter to quantify the stability of a set of materials. According to the definition, the Morton number can be assumed as a ratio between the viscous force over the inertia to the surface tension forces. It is well known that viscous forces tend to keep the system stable,

$$Mo = \frac{g \cdot \mu_c^4 \cdot \Delta\rho}{\rho_c^2 \cdot \gamma^3} = \frac{F_v}{F_{st} \cdot F_i}. \quad (30)$$

The line tends to be steeper in low Morton regions, such as the liquid metal region (Fig. 9). The stability line becomes more and more independent of the Morton number, and the Eötvös number at which instabilities occur becomes a constant. The viscous effect is negligible in this region, and the stability is only controlled by the balance between the inertia and the surface tension forces (Morton number).

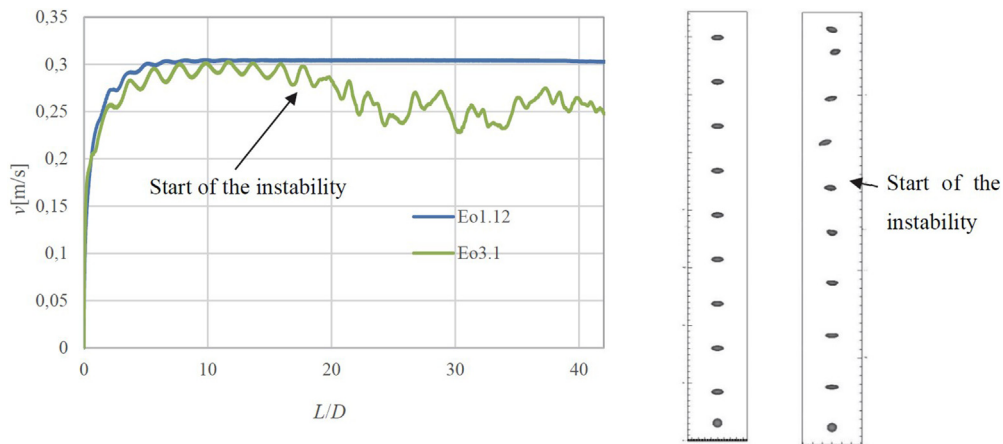


FIG. 8. Right: Velocity for $Eo = 1.12$ and 3.1 bubbles. Left: x - z section of bubble trajectory (left: $Eo = 1.12$ right: $Eo = 3.1$).

Since the Weber and Eötvös numbers are connected, the stability can also be expressed as a function of the Eötvös number,

$$Stability = f\left(\frac{F_i}{F_{st}}\right) = f(We(Eo)) = g(Eo). \quad (31)$$

The region in which the bubble passes from a spherical-like body to a wobbling disk for different material properties has been investigated. Figure 10 suggests that the transition happens almost at the same Eötvös number for all three metals ($Eo = 1.7$). This is further proof that this process is not influenced by the Morton number, because the viscosity effects are negligible, compared to the inertia and superficial ones.

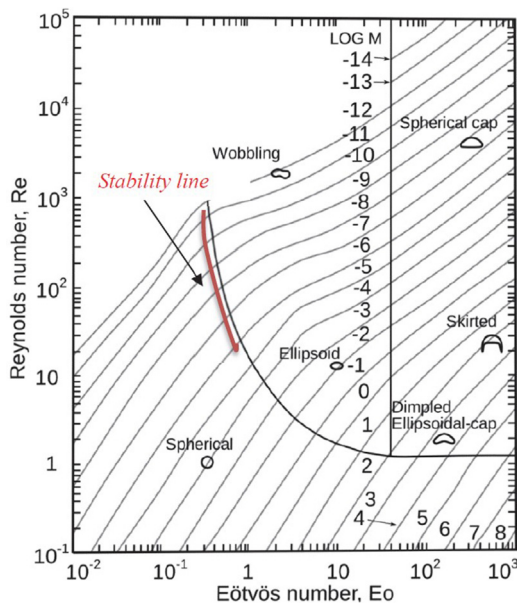


FIG. 9. Grace diagram (Acrivos, 1979).

NOVEL CORRELATION FOR BUBBLE ASPECT RATIO

At the beginning of the simulation, the bubble is into a quiescent liquid, and it has a spherical shape. The bubble starts to rise, due to an unbalance of the gravity and Archimedes force.

As the bubble rises with increasing velocity, hydrodynamic pressure due to metal flow at the top of the bubble increases. Due to the incompressibility constraint, bubble compression at the top and bottom leads to elongation at the sides, and the bubble shape becomes elliptic.

Moore (1959) proposed a simple correlation for the bubble aspect ratio X , which is valid for spherical-like bubbles, but loses its applicability for higher Weber numbers:

$$X = 1 + \frac{9}{64} \cdot We + O(We^2). \quad (32)$$

In analytical theory, we propose a new semi-analytical method for the aspect ratio of a bubble rising in liquid metals. The bubble aspect ratio depends only on the total pressure field on the bubble surface. Since $Re \gg 1$, the viscous pressure is neglected, with respect to the kinetic pressure, and the inviscid approximation, thus, becomes reasonable.

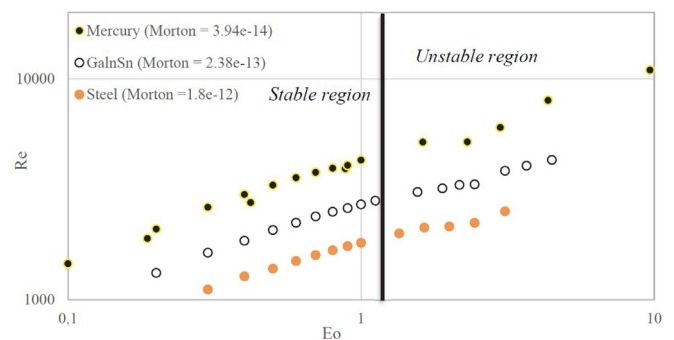


FIG. 10. Reynolds vs Eötvös for bubbles rising in different liquid metals.

Analytical theory

Force balance and curvature

Once the bubble has reached its terminal velocity, the acceleration of the system is zero and the bubble and all its components are in force equilibrium ($\sum F = 0$). The force balance of a bubble interface can be calculated if the inner and the outer pressure are known, as illustrated in Fig. 11.

The force balance in each moment (νt) can be expressed by

$$p_{in} = p_{out} + \gamma\chi. \tag{33}$$

Since the velocity field is zero at the beginning of the rise ($t = 0$), Eqs. (34) and (35), can be asserted:

$$p_{in} = \gamma\chi_0 + \rho gh. \tag{34}$$

$$p_{in} - \rho gh = \gamma\chi_0 = \frac{4\gamma}{D}. \tag{35}$$

The outer pressure is found by applying the Navier–Stokes equations along a streamline from the non-perturbed region to the interface, Eq. (36). Since the viscous effect is negligible, the flow field can, therefore, be approximated as an irrotational field ($\nabla \times \vec{u} = 0$). The energy inside the fluid is conserved. The total outer pressure is the sum of the gravitational pressure, ρgh and the kinetic pressure, $\frac{1}{2}\rho(u_\infty^2 - u^2)$. The gravitation force is not technically constant, since it depends on the depth of the liquid, but for simplification reasons, it was set constant to ρgh , with h being the depth of the bubble center of the mass. Assuming that the fluid is almost perfectly inviscid, there are no interface boundary layers and the interface tangential liquid velocity is non-zero ($u_{//}(s) \neq 0, u_r(s) = 0$),

$$p_{out}(s) = \rho gh + \frac{1}{2}\rho(u_\infty^2 - u^2(s)). \tag{36}$$

The inner pressure can easily be computed by applying the Navier–Stokes equations to the inner gas. Basically, the pressure field inside the bubble is spatially almost constant, that is, $\nabla p = 0$.

Once the bubble has reached its terminal velocity, the shape remains constant, which means that the bubble curvature is kept

constant at each point. In the same way, the velocity field across the bubble does not change. The gravitational term linearly decreases during rising of the bubble, since the depth is decreasing $\rho g[h - u_\infty \cdot t]$. The inner gas pressure also decreases to keep the system stable and to provide force balance at each point in time. Therefore, the $p_{in}(t) - \rho gh(t)$ term is a constant during bubble rising,

$$\chi(s) = \frac{\frac{1}{2}\rho u^2(s) + \rho gh - p_{in} - \frac{1}{2}\rho u_\infty^2}{\gamma}. \tag{37}$$

Equation (37) suggests that the local interface curvature is linearly dependent on the kinetic pressure and inversely proportional to the surface tension coefficient. Furthermore, $\rho gh - p_{in} - \frac{1}{2}\rho u_\infty^2$ is constant for each point of the interface. Therefore, the driving factor to compute the curvature is the interface tangential velocity field, $u_{//}(s)$. In order to obtain the ideal resolution of the bubble shape problem, inviscid Euler equations have to be solved around the bubble to find the tangential velocity, $u_{//}$, to the surface, as this is needed to calculate the bubble curvature, $\chi(s)$, according Eq. (37).

Here, an equivalent method, which avoids the need to solve the Euler equations for the ellipsoidal coordinates and provides an accurate correlation for stable ellipsoidal bubbles in inviscid liquid, is proposed.

Let us now consider the bubble at the first instant in which it is quiescent and has a perfect spherical shape. In this situation, the velocity field is zero, and the main driven force is the Archimedes force

Nevertheless, for simplicity, the hydrostatic pressure is set equal to ρgh for the bubble aspect ratio calculation on the entire interface, since $h \gg D$, and the relative difference between p_{up} and p_{down} is negligible. Setting the hydrostatic pressure constant is a reasonable approximation to compute the bubble shape. However, it cannot be assumed in the momentum balance equation because the difference between the upper and lower hydrostatic pressures is the driving factor behind the rise in the bubble. If the hydrostatic pressure is assumed to be constant, the bubble is in static equilibrium. It can be established, from the balance of the forces acting on the surface at $t = 0$ (Fig. 11), that $p_{out} - \rho gh$, which was previously demonstrated to remain constant during bubble rising, is equal to the initial curvature overpressure, $\gamma\chi_0$,

$$p_{in} - \rho gh = \gamma\chi_0. \tag{38}$$

Using Eqs. (37) and (38), the final balance equation on the interface [Eq. (39)] shows how the local curvature behaves. It is equal to an initial constant value plus a kinetic pressure dependent value. It is clear that the velocity field is the only factor that influences the local bubble curvature. Regions with high kinetic pressure result in a low curvature interface, and vice versa. Ideally, the velocity field $u(s)$ can be found by solving the Euler equations for the ellipsoidal shape and it clearly depends on the local curvature $u(s) \rightarrow u(s, \chi(s))$ of the bubble. This process tends to become complex and long,

$$\gamma\chi(s) = \gamma\chi_0 + \frac{1}{2}\rho(u^2(s) - u_\infty^2). \tag{39}$$

Curvature at the top of the bubble

In our analysis, the bubble shape was considered to be a perfect ellipsoid ($\frac{x^2}{a^2} + \frac{y^2}{b^2} + \frac{z^2}{c^2} = 1$). Since the flow is axisymmetric, the

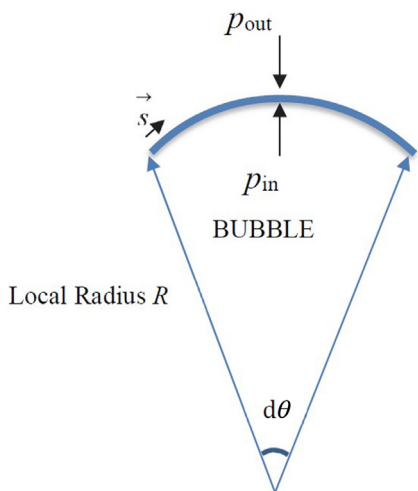


FIG. 11. Force balance on the bubble interface.

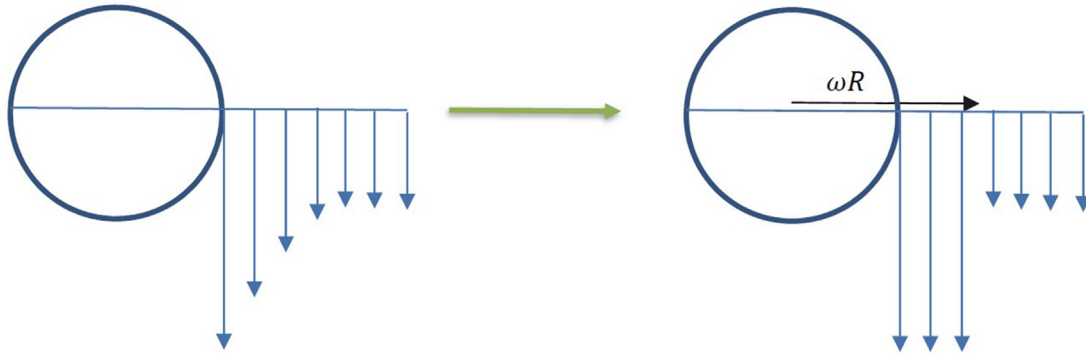


FIG. 12. Difference between real side velocity field and modeled one for a spherical body (x-z or y-z).

bubble shape in the x and y directions is the same ($a = b$) and the ellipsoid can be perfectly characterized by only the a and c parameters. To characterize the problem, it is only necessary to solve the curvature equation at two different points on the bubble, since there are only two unknowns. The first point considered is the bubble stagnation point in which the kinetic pressure is the highest, Eq. (40). Here, the fluid stops, and all the kinetic energy is transmuted into pressure. This is a convenient solution point since here the velocity is zero for any aspect ratio,

$$\chi_{\min} = \chi(\theta = 0) = \chi_o - \frac{1}{2} \frac{\rho \cdot u_{\infty}^2}{\gamma}. \quad (40)$$

Curvature at the side of the bubble

The second point that was considered is the one with the highest curvature, which occurs at an angle of 90° , with the curvature being defined as

$$\chi_{\max} = \chi\left(\theta = \frac{\pi}{2}\right) = \chi_o + \frac{1}{2} \frac{\rho}{\gamma} \cdot \left(u^2\left(\frac{\pi}{2}\right) - u_{\infty}^2\right). \quad (41)$$

Here, the fluid velocity, to satisfy conservation of the mass ($\nabla \cdot u = 0$), increases, with a consequent production of a negative kinetic pressure on the interface, which, in turn, stretches the bubble. How the tangential velocity behaves at each other point is not of interest since only the largest and the smallest curvatures are needed. The major problem is to find the tangential velocity at 90° .

Tangential velocity field

First, from the solution of the Euler equations in the spherical coordinates, only the tangential component of the velocity is present on the interface, and not the radial one. In a perfect spherical case, $u_{\theta}\left(\frac{\pi}{2}\right) = \frac{3}{2} u_{\infty}$.

Equations (42) and (43) are Euler incompressible equations for mass and momentum conservation, respectively,

$$\nabla \cdot u = 0, \quad (42)$$

$$\rho \cdot \frac{\partial u}{\partial t} + \rho \cdot (u \cdot \nabla)u = -\nabla p + \rho g. \quad (43)$$

Equations (44) and (45) are the radial and tangential velocity field solutions of the Euler incompressible equations,

$$u_r(r, \theta) = u_{\infty} \left(1 - \frac{R^3}{r^3}\right) \cos(\theta), \quad (44)$$

$$u_{\theta}(r, \theta) = -u_{\infty} \left(1 + \frac{R^3}{2r^3}\right) \sin(\theta). \quad (45)$$

In an ideal case, the tangential velocity decreases ($\propto \frac{1}{r^3}$) from $\frac{3}{2} u_{\infty}$ to u_{∞} , moving away from the sphere. An equivalent model is used for the ellipsoidal bubble in which, for a certain range, the velocity is uniformly constant and equal to the interface tangential velocity (Fig. 12). We assume that, after a certain distance, the flow is no longer perturbed by the presence of the sphere (Fig. 12). Nevertheless, the velocity is considered spatially uniform in the perturbed region and equal to the tangential velocity at the interface [Eq. (46)]. The key point is to find the distance beyond which the velocity drops from the tangential velocity value to zero. The distance has been decided imposing that all liquid momentum of the real case is confined only in the perturbed range in the modeled case. In view of integral volume flow rate conservation (Fig. 13), the ideal “perturbed range” can be found for a spherical bubble [Eq. (47)] and it is equal to $\sqrt{3} \cdot R$.

ω is defined as the ratio between the distance from the center of the bubble at which the flow starts to become unperturbed to the side radius of the bubble,

$$\pi(\omega R)^2 \cdot u_{\infty} = \pi[(\omega R)^2 - R^2] \cdot \frac{3}{2} u_{\infty}, \quad (46)$$

$$\omega = \sqrt{3}. \quad (47)$$

This approach can also be used for ellipsoidal bubbles, but with some geometrical corrections. V_{tot} is the total volume of the bubble, and it is

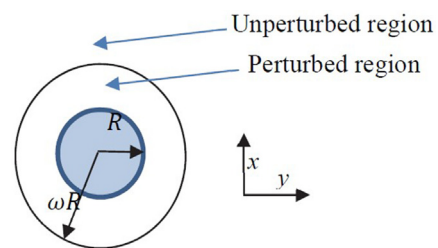


FIG. 13. Top view of a spherical bubble.

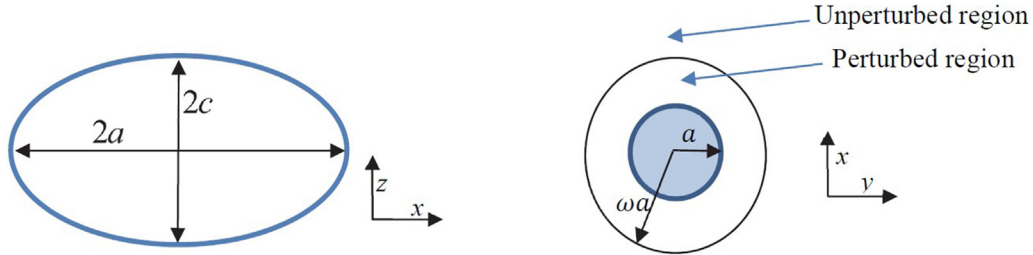


FIG. 14. On the left, side representation of the ellipsoidal bubble, on the right top view of the ellipsoidal bubble.

kept constant during the rise since no breakup phenomena take place. The width of the bubble is dependent on its characteristic diameter ($D = \sqrt[3]{\frac{6 \cdot V_{inf}}{\pi}}$) and on the bubble aspect ratio ($X = \frac{a}{c}$). Using the current definitions, and assuming that the bubble volume does not change under compression, the width is found as a function of the initial diameter and the aspect ratio,

$$a = D \cdot \sqrt[3]{\frac{X}{8}} \tag{48}$$

Volume flow rate conservation [Eq. (49)] is applied to an ellipsoidal bubble (Fig. 14) to determine the liquid side velocity $u(\frac{\pi}{2})$, Eq. (50),

$$\pi(\omega a)^2 \cdot u_\infty = \pi[(\omega a)^2 - a^2] \cdot u\left(\frac{\pi}{2}\right), \tag{49}$$

$$u\left(\frac{\pi}{2}\right) = u_\infty \cdot \frac{\omega^2}{\omega^2 - 1}. \tag{50}$$

In the ellipsoidal case, finding ω is the key point since it is only known *a priori* in the spherical case. We assume that ω is a function of aspect ratio X , which is always greater than unity, and $\omega(X = 1) = \sqrt{3}$. It is generally known that $u_{//}(\frac{\pi}{2})$ is higher in highly distorted bubbles, since a larger amount of fluid is deflected as a result of the presence of the bubble and this fluid flows entirely on the side of the bubble, $\frac{du(\pi/2)}{dX} > 0$. Terminal bubble velocity u_∞ decreases slightly as the aspect ratio increases, since the drag coefficient is higher for highly distorted bubbles: $\frac{du_\infty}{dX} < 0$. Therefore, according to Eq. (51), $\omega^2/(\omega^2 - 1)$ increases with X . By solving Eq. (52), it is possible to prove that $\omega(X)$ monotonously decreases with X , Eq. (53). Furthermore, $\omega(X)$ only reaches 1 asymptotically (Fig. 15),

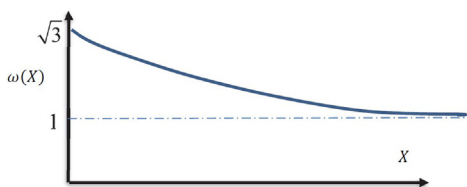


FIG. 15. Possible omega function (the ratio between the distance from the center of the bubble at which the flow starts to become unperturbed to the side radius of the bubble).

$$\frac{d\left(\frac{\omega^2}{\omega^2 - 1}\right)}{dX} = \frac{d\left(\frac{u(\pi/2)}{u_{inf}}\right)}{dX} = \frac{\left(\frac{du(\pi/2)}{dX}\right) \cdot u_{inf} - \left(\frac{du_{inf}}{dX}\right) \cdot u(\pi/2)}{u_{inf}^2} > 0, \tag{51}$$

$$\frac{d\frac{\omega^2}{\omega^2 - 1}}{dX} = \frac{2\omega \cdot \frac{d\omega}{dX} \cdot (\omega^2 - 1) - \omega^2 \cdot 2\omega \cdot \frac{d\omega}{dX}}{(\omega^2 - 1)^2} = \frac{d\omega}{dX} \cdot \frac{(-2\omega)}{(\omega^2 - 1)^2} > 0, \tag{52}$$

$$\frac{d\omega}{dX} < 0. \tag{53}$$

For practical calculations, it was hypothesized that $\omega(X)$ follows a decrease that is proportional to $\frac{1}{X^n}$, as can be seen in Eq. (54). Under this assumption, the function is controlled by the n parameter, which is an unknown, while n represents how fast the function tends to 1. The latter is a free parameter that is guessed by comparing the theory with the PSI-BOIL simulation,

$$\omega(X) \approx \frac{(\sqrt{3} - 1)}{X^n} + 1. \tag{54}$$

Curvature calculation

According to the previous consideration, higher curvature [Eq. (55)] and lower curvature [Eq. (56)] can be calculated and correspond to $\frac{\pi}{2}$ and the 0 angle, respectively,

$$\chi_{max} = \chi\left(\frac{\pi}{2}\right) = \frac{4}{D} - \frac{1}{2} \cdot \frac{\rho \cdot u_\infty^2}{\gamma} \cdot \left(1 - \left(\frac{\omega^2(X)}{\omega^2(X) - 1}\right)^2\right), \tag{55}$$

$$\chi_{min} = \chi(0) = \frac{4}{D} - \frac{1}{2} \cdot \frac{\rho \cdot u_\infty^2}{\gamma}. \tag{56}$$

The analytical expression of the aspect ratio of an ellipsoid can be found from the different calculations (Fig. 16). In our case, the velocity field and the bubble shape are axisymmetric. In fact, there is no dependence of any variable on $0 < \varphi < 2\pi$ ($a = b$).

The side [Eq. (57)] and the top [Eq. (58)] curvatures of a 3D ellipsoid can be analytically expressed as a function of the ellipsoidal aspect ratio (X) and the semi-major axis (a). Equation (59) is obtained from the ratio of Eqs. (58) to (57),

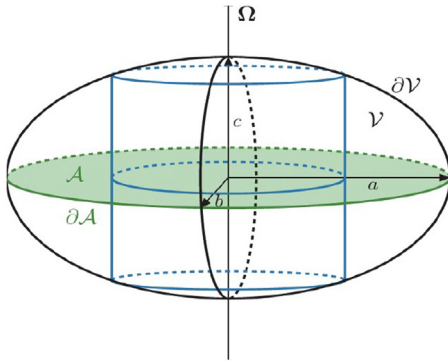


FIG. 16. Ellipsoidal representation of the bubble.

$$\chi_{\max} = \frac{1}{R_s} + \frac{1}{R_t} = \frac{a}{c^2} + \frac{1}{a} = \frac{\left(\frac{a}{c}\right)^2 + 1}{a} = \frac{X^2 + 1}{a}, \quad (57)$$

$$\chi_{\min} = \frac{1}{R_s} + \frac{1}{R_t} = \frac{c}{a^2} + \frac{c}{a^2} = \frac{2}{a} \cdot \frac{c}{a} = \frac{2}{a \cdot X}, \quad (58)$$

$$\frac{\chi_{\min}}{\chi_{\max}} = \frac{\left(\frac{2}{a \cdot X}\right)}{\left(\frac{X^2 + 1}{a}\right)} = \frac{2}{X(X^2 + 1)}. \quad (59)$$

Substituting the definition of the max. and min. curvature for bubbles [Eqs. (55) and (56)] in Eq. (58), an explicit correlation between the Weber number and the bubble aspect ratio [Eq. (63)] is found. This is a proof that the bubble deformation in inviscid fluids is only controlled by the ratio of the inertia to the surface tension forces.

Let us define $F(X)$ as Eq. (60) for compactness reasons,

$$F(X) = \frac{\omega^2(X)}{\omega^2(X) - 1}, \quad (60)$$

$$\frac{\chi_{\min}}{\chi_{\max}} = \frac{2}{X \cdot (X^2 + 1)} = \frac{4 - \frac{1}{2} \cdot \frac{\rho \cdot u_{\infty}^2 \cdot D}{\gamma}}{4 - \frac{1}{2} \cdot \frac{\rho \cdot u_{\infty}^2 \cdot D}{\gamma} \cdot (1 - F^2(X))}, \quad (61)$$

$$\frac{\chi_{\min}}{\chi_{\max}} = \frac{2}{X \cdot (X^2 + 1)} = \frac{4 - \frac{1}{2} We}{4 - \frac{1}{2} We \cdot (1 - F^2(X))}, \quad (62)$$

$$We = \frac{16 - 8X \cdot (X^2 + 1)}{2 \cdot (1 - F^2(X)) - X \cdot (X^2 + 1)}. \quad (63)$$

Once $\omega(X)$ has been estimated, the correlation can successfully be used in Eq. (63). If we linearize the function in the surroundings of $X = 1$, the Moore linear correlation is found.

Moreover, the omega function cannot be known *a priori*, unless the Euler equations are analytically solved in ellipsoidal coordinates. This formula is valid as long as the bubble shape can be considered an ellipsoid. When the top curvature becomes zero, the ellipsoidal aspect ratio mathematically diverges to infinity. In order to keep this theory valid, the top curvature has to be greater than zero, Eq. (64). This

condition is achieved when the Weber number of a bubble is less than 8, Eq. (65). However, this limit is practically never reached because the bubble becomes unstable much sooner ($We \sim 4$),

$$\chi_{TOP} = \frac{4}{D} - \frac{1}{2} \cdot \frac{\rho \cdot u_{\infty}^2}{\gamma} \gg 0, \quad (64)$$

$$We \ll 8. \quad (65)$$

Comparison of the aspect ratio of the analytical solution to PSI-BOIL

The following analytical solution has been compared with the CFD results to determine the n parameter that fully characterizes the omega function, $\omega(X)$ [Eq. (66)]. Aspect ratio X was calculated for 30 simulations for three different sets of materials (argon+steel, argon+GaInSn, and nitrogen+mercury) within the $0.1 < Eo < 1.2$ range.

Unfortunately, the bubble shape is more sensitive than the terminal velocity to the grid size. The relative error of the aspect ratio clearly depends on the $\frac{\Delta x}{R_{\min}} = \Delta x \cdot \chi_{\max}$ ratio, which represents how well the grid manages to represent the bubble interface at the point with the highest curvature on the side of the bubble.

Grid sensitivity studies were conducted for an $Eo = 0.5$ bubble, and the relative error pertaining to the aspect ratio was almost 10%, compared to an ultrafine grid simulation where a spatial resolution of 50 cells on the bubble diameter has been adopted ($D/dx = 50$). Furthermore, it was observed that the lack of accuracy of the grid always leads to an underestimation of the aspect ratio. Even though the relative error is lower for small bubbles, since they are less stretched, a conservative analysis was adopted, and a 10% relative error was set for all the points.

The best interpolation was found for $n = 1.34$. Exponential fitting has been performed with $R^2 = 0.92$,

$$\omega(X) \approx \frac{(\sqrt{3} - 1)}{X^{1.34}} + 1, \quad (66)$$

$$F(X) = \frac{\omega^2(X)}{\omega^2(X) - 1}, \quad (67)$$

$$We = \frac{16 - 8X \cdot (X^2 + 1)}{2 \cdot (1 + F^2(X)) - X \cdot (X^2 + 1)}. \quad (68)$$

Equation (68) precisely predicts the bubble aspect ratio in an inviscid regime (Fig. 17). It is applicable to bubble rising in liquid metal for $0 < Eo < 1.2$. However, above $Eo = 1.2$, the bubble becomes unstable, the shape is no longer ellipsoidal and the theory is no longer valid.

CONCLUSIONS

In this study, Computational Fluid Dynamics (CFD) simulation has been used to improve knowledge of a bubble rising in liquid metals. More precisely, the bubble rising velocity and the bubble deformation were investigated using the CFD code, that is, PSI-BOIL.

A rising bubble in liquid metal was studied, and the predicted terminal rising velocity was compared with Tomiyama's correlation. The simulation results showed that the drag coefficient is only controlled by the Eötvös number for large bubbles and shows the same tendency as Tomiyama's correlation. A semi-analytical model for bubble shape deformation was then derived for liquid metal and compared with the

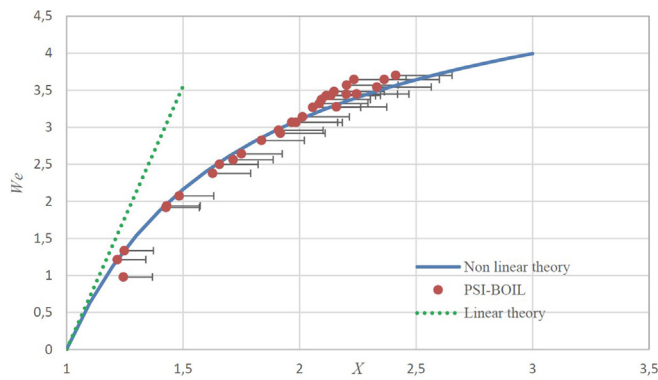


FIG. 17. Comparison between linear and nonlinear theory for inviscid liquid.

simulation results. The result shows that inviscid approximation works well for bubbles in liquid metal and that the bubble aspect ratio is only controlled by the Weber number. Furthermore, a new stability criterion for bubbles in a liquid metal has been proposed. In the proposed criterion, bubble stability in the considered liquid metal was not controlled by the Morton number, but only by the Eötvös number. Transition from an ellipsoidal to a wobbling disk shape took place for the fixed Eötvös number ($Eu = 1.7$). The novelty is the formulation of a stability criterion for high Reynolds ($1000 < Re < 10\,000$) bubble stability for which experimental correlation are hardly achievable.

As a follow-up of this article, further studies on bubble aspect ratio are going on. Simulations on bubble rising in metals under magnetic field (horizontal and vertical) to study bubble shape, trajectory, and velocity are also planned.

ACKNOWLEDGMENTS

This study has been supported by the Paul Scherrer Institute (LSM department) in collaboration with ETH Zurich (D-MAVT).

AUTHOR DECLARATIONS

Conflict of Interest

The authors have no conflicts to disclose.

Author Contributions

Marino Corrado: Conceptualization (lead).

DATA AVAILABILITY

The data that supports the findings of this study are available within the article.

REFERENCES

- Acrivós, A., “Bubbles, drops and particles. By R. Clift, J. R. Grace and M. E. Weber. Academic Press, 1978. 380 pp. £20.80 or \$32.00,” *J. Fluid Mech.* **94**(4), 795–796 (1979).
- Aoyama, S., Hayashi, K., Hosokawa, S., and Tomiyama, A., “Shapes of ellipsoidal bubbles in infinite stagnant liquids,” *Int. J. Multiphase Flow* **79**, 23–30 (2016).

- Baake, E., Fehling, T., Musaeva, D., and Steinberg, T., “Neutron radiography for visualization of liquid metal processes: Bubbly flow for CO₂ free production of hydrogen and solidification processes in EM field,” *IOP Conf. Ser. Mater. Sci. Eng.* **228**, 012026 (2017).
- Besagni, G. and Deen, N. G., “Aspect ratio of bubbles in different liquid media: A novel correlation,” *Chem. Eng. Sci.* **215**, 115383 (2020).
- Birjukovs, M., Dzelme, V., Jakovics, A., Thomsen, K., and Trtik, P., “Phase boundary dynamics of bubble flow in a thick liquid metal layer under an applied magnetic field,” *Phys. Rev. Fluids* **5**(6), 061601 (2020).
- Birjukovs, M., Trtik, P., Kaestner, A., Hovind, J., Klevs, M., Gawryluk, D. J., Thomsen, K., and Jakovics, A., “Resolving gas bubbles ascending in liquid metal from low-SNR neutron radiography images,” *Appl. Sci.* **11**(20), 9710 (2021).
- Cano-Lozano, J. C., Bohorquez, P., and Martínez-Bazán, C., “Wake instability of a fixed axisymmetric bubble of realistic shape,” *Int. J. Multiphase Flow* **51**, 11–21 (2013).
- Gaudlitz, D. and Adams, N. A., “Numerical investigation of rising bubble wake and shape variations,” *Phys. Fluids* **21**(12), 122102 (2009).
- Haas, T., Schubert, C., Eickhoff, M., and Pfeifer, H., “A review of bubble dynamics in liquid metals,” *Metals* **11**(4), 664 (2021).
- Jin, K., Kumar, P., Vanka, S. P., and Thomas, B. G., “Rise of an argon bubble in liquid steel in the presence of a transverse magnetic field,” *Phys. Fluids* **28**(9), 093301 (2016).
- Hadamard, J. S., “Mouvement permanent lent d’une sphere liquide et visqueuse dans un liquide visqueux,” *C.R. Acad. Sci.* **152**, 1735 (1911).
- Kang, I. S. and Leal, L. G., “The drag coefficient for a spherical bubble in a uniform streaming flow,” *Phys. Fluids* **31**(2), 233–237 (1988).
- Keplinger, O., Shevchenko, N., and Eckert, S., “Validation of x-ray radiography for characterization of gas bubbles in liquid metals,” *IOP Conf. Ser. Mater. Sci. Eng.* **228**, 012009 (2017).
- Keplinger, O., Shevchenko, N., and Eckert, S., “Visualization of bubble coalescence in bubble chains rising in a liquid metal,” *Int. J. Multiphase Flow* **105**, 159–169 (2018).
- Keplinger, O., Shevchenko, N., and Eckert, S., “Experimental investigation of bubble breakup in bubble chains rising in a liquid metal,” *Int. J. Multiphase Flow* **116**, 39–50 (2019).
- Krull, B., Tschisgale, S., and Fröhlich, J., “An immersed boundary method for complex-shaped bubbles represented by spherical harmonic functions,” in 9th International Conference on Multiphase Flow, 2016.
- Legendre, D., Zenit, R., and Velez-Cordero, J. R., “On the deformation of gas bubbles in liquids,” *Phys. Fluids* **24**(4), 043303 (2012).
- Liu, Z. and Li, B., “Large-eddy simulation of transient horizontal gas–liquid flow in continuous casting using dynamic subgrid-scale model,” *Metall. Mater. Trans. B* **48**(3), 1833–1849 (2017).
- Lorenzin, N. and Abánades, A., “A review on the application of liquid metals as heat transfer fluid in concentrated solar power technologies,” *Int. J. Hydrogen Energy* **41**(17), 6990–6995 (2016).
- Mendelson, H. D., “The prediction of bubble terminal velocities from wave theory,” *AIChE J.* **13**(2), 250–253 (1967).
- Moore, D. W., “The rise of a gas bubble in a viscous liquid,” *J. Fluid Mech.* **6**, 113–130 (1959).
- Mori, Y., Hijikata, K., and Kuriyama, I., “Experimental study of bubble motion in mercury with and without a magnetic field,” *J. Heat Transfer* **99**(3), 404–410 (1977).
- Mougin, G. and Magnaudet, J., “Path instability of a rising bubble,” *Phys. Rev. Lett.* **88**, 014502 (2001).
- Richter, T., Keplinger, O., Shevchenko, N., Wondrak, T., Eckert, K., Eckert, S., and Odenbach, S., “Single bubble rise in GaInSn in a horizontal magnetic field,” *Int. J. Multiphase Flow* **104**, 32–41 (2018).
- Schwarz, S. and Fröhlich, J., “Numerical study of single bubble motion in liquid metal exposed to a longitudinal magnetic field,” *Int. J. Multiphase Flow* **62**, 134–151 (2014).
- Strumpf, E., “Experimental study on rise velocities of single bubbles in liquid metal under the influence of strong horizontal magnetic fields in a flat vessel,” *Int. J. Multiphase Flow* **97**, 168–185 (2017).
- Timmel, K., Eckert, S., Gerbeth, G., Stefani, F., and Wondrak, T., “Experimental modeling of the continuous casting process of steel using low melting point metal alloys—the LIMMCAST program,” *ISIJ Int.* **50**(8), 1134–1141 (2010).

- Tomiyama, A., Celata, G. P., Hosokawa, S., and Yoshida, S., "Terminal velocity of single bubbles in surface tension force dominant regime," *Int. J. Multiphase Flow* **28**(9), 1497–1519 (2002).
- Tomiyama, A., Kataoka, I., Zun, I., and Sakaguchi, T., "Drag coefficients of single bubbles under normal and micro gravity conditions," *JSME Int. J., Ser. B* **41**(2), 472–479 (1998).
- Wang, Z. H., Wang, S. D., Meng, X., and Ni, M. J., "UDV measurements of single bubble rising in a liquid metal Galinstan with a transverse magnetic field," *Int. J. Multiphase Flow* **94**, 201–208 (2017).
- Will, J. B., Mathai, V., Huisman, S. G., Lohse, D., Sun, C., and Krug, D., "Kinematics and dynamics of freely rising spheroids at high Reynolds numbers," *J. Fluid Mech.* **912**, A16 (2021).
- Yan, X., Zheng, K., Jia, Y., Miao, Z., Wang, L., Cao, Y., and Liu, J., "Drag coefficient prediction of a single bubble rising in liquids," *Ind. Eng. Chem. Res.* **57**(15), 5385–5393 (2018).
- Yang, W., Luo, Z., Gu, Y., Liu, Z., and Zou, Z., "Numerical analysis of effect of operation conditions on bubble distribution in steel continuous casting mold with advanced bubble break-up and coalescence models," *ISIJ Int.* **60**(10), 2234–2245 (2020).
- Zhang, C., Eckert, S., and Gerbeth, G., "Experimental study of single bubble motion in a liquid metal column exposed to a DC magnetic field," *Int. J. Multiphase Flow* **31**(7), 824–842 (2005).
- Zhang, J. and Ni, M.-J., "Direct simulation of single bubble motion under vertical magnetic field: Paths and wakes," *Phys. Fluids* **26**(10), 102102 (2014).
- Zhang, J., Ni, M.-J., and Moreau, R., "Rising motion of a single bubble through a liquid metal in the presence of a horizontal magnetic field," *Phys. Fluids* **28**(3), 032101 (2016).
- Zhang, J., Sahu, K. C., and Ni, M.-J., "Transition of bubble motion from spiralling to zigzagging: A wake-controlled mechanism with a transverse magnetic field," *Int. J. Multiphase Flow* **136**, 103551 (2021).
- Zhou, W. and Dušek, J., "Marginal stability curve of a deformable bubble," *Int. J. Multiphase Flow* **89**, 218–227 (2017).
- Zhou, Y., Zhao, C., and Bo, H., "Analyses and modified models for bubble shape and drag coefficient covering a wide range of working conditions," *Int. J. Multiphase Flow* **127**, 103265 (2020).